Results in Engineering 24 (2024) 103567

Contents lists available at ScienceDirect

Results in Engineering

journal homepage: www.sciencedirect.com/journal/results-in-engineering

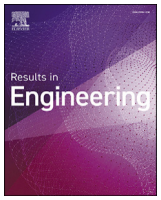

Research paper

Effect of mushy zone constant in Voller-Prakash model on keyholing behaviour in laser powder bed fusion simulation

Jun Katagiri, Sukeharu Nomoto, Masahiro Kusano, Makoto Watanabe *

Additive Manufacturing Group, Research Center for Structural Materials, National Institute for Materials Science, Sengen 1-2-1, Tsukuba, 305-0047, Ibaraki, Japan

ARTICLE INFO

Keywords:
Laser powder bed fusion
Mushy zone flow resistance
Voller-Prakash model
Multiphysics CFD simulation
Keyhole pore formation

ABSTRACT

This paper is a study of the model constant of the Voller-Prakash model: the mushy zone constant (C), which determines the flow resistance in the mushy zone during metal solidification. A drag force-liquid fraction relation was derived, assuming that the dynamic and static pressures were equal. The C values for the three morphologies were estimated by analytically calculating the morphological parameters of the Kozeny-Carman equation, which was the basis of the Voller-Prakash model. As a result, much smaller values of C were obtained compared to the commonly used range of $C > 10^5$. This was due to the drag force model included a parameter related to the grid size of the simulation. Based on previous studies of the scale of the dendrite structure and the grid size widely used in simulations, we concluded that the rectangular morphology was reasonable. To evaluate the effect of C value on keyholing behaviour, a series of the multiphysics CFD simulations was performed varying C, including the C for rectangular morphology and the commonly-used C from past studies. The flow resistance force in the mushy zone increased with larger C values, resulting in significant restriction of pore displacement. Consequently, pores formed with smaller C values were immobilised farther away from the laser position. For larger values of C, the flow resistance force had a significant effect, causing the mushy zone to behave like a solid. The pores that formed were trapped by the solid-like mushy zone before they could reach a stable shape and size.

1. Introduction

Laser powder bed fusion (L-PBF) is a type of metal 3D additive manufacturing technology. Its advantage is that it can easily produce complex-shaped parts compared to conventional metal manufacturing processes. As L-PBF is a new processing technology, there are many unclear factors that affect the production of high-quality parts. Therefore, extensive research and development of L-PBF is being conducted worldwide. Note that there are a number of different additive manufacturing techniques. One of the most representative techniques is the fused deposition method (FDM). Researches and developments for the FDM have been extensively performed in the past studies. For example, Manola et al. have applied machine learning for optimisation of process parameters in the FDM [1]. Ramlee et al. have evaluated effect of post-printing material on mechanical property and reported that cement-reinforced printed object exhibited higher strength than the objects reinforced with the other materials [2]. Lestari et al. have investigated the impact of the FDM process parameters on printing time and weight of printed objects, and optimised the process parameters using the Taguchi method and the response surface method [3]. Moreover, Nagaraja et al. have reviewed the utilisation of natural materials such as in the additive manufacturing [4]. Abd Aziz et al. have used the 3D printer for validation of the finite element method (FEM) simulations of mechanical properties of 3D scanned femur model [5]. Following the direct comparison of the FEM and experiment, they evaluated fixation methods for femur fractures based on the FEM simulations.

The defects generated strongly depend on the laser processing conditions (laser power and scanning speed). A process map or process window, which is a diagram illustrating the defects produced by combining these two variables, is crucial for practical manufacturing [6]. It is important to determine the process window before manufacturing the product, as it varies depending on the material used. Generating the process window is a time-consuming task that involves single track experiments at different laser powers and scan speeds, track cutting and polishing, and SEM observation. To assist the experimental observation, multi-physics computational fluid dynamics (CFD) simulation of L-PBF has been extensively studied. Such simulations have advantages such as the ability to observe physical quantities that are difficult to observe

* Corresponding author.
E-mail address: WATANABE.Makoto@nims.go.jp (M. Watanabe).

https://doi.org/10.1016/j.rineng.2024.103567
Received 23 January 2024; Received in revised form 8 August 2024; Accepted 26 November 2024

Available online 2 December 2024

in experiments. Moreover, these numerical simulations, in conjunction with computer-aided design (CAD), offer a further notable advantage: they can significantly accelerate the design and prototype testing processes. For example, in the biomedical field, there have been studies that have employed FEM-based mechanical simulations to investigate materials and designs for total hip replacement techniques [7–9]. Moreover, the FEM [10] and TRIZ-based techniques [11] have been utilised in the design and development of mechanical components for surgical chairs. Note that CFD is a simulation method that is widely used in the design and prototyping processes across a broad range of industries, not only the metal 3D additive manufacturing but also mechanical [12,13] and the biomedical industries [14–16].

The L-PBF is a complex multi-physics phenomenon involving heat conduction with melting and solidification, thermo-fluid dynamics of the molten metal, laser heating and powder particle dynamics. Such simulations require the coupling of several physical models. The coupling simulation of heat transfer, fluid dynamics and laser heating has been performed in previous numerous studies, e.g., [17–25]. Note that this study focuses on defect formation during metal solidification in L-PBF fabrication. The other type of simulation, e.g. thermo-elasto-plastic mechanical simulations, were also performed to evaluate the residual deformation after L-PBF fabrication [26] and solidification crack [27]. In other cases, finite element simulation of heat transfer, taking into account melting and solidification, is used to evaluate molten pool dimensions (e.g. molten pool width and depth) [6,28]. Thus, numerical simulation is becoming an essential tool for evaluating the phenomena occurring during L-PBF fabrication.

The multiphysics CFD simulation naturally uses several sets of governing equations and a variety of physical models. Among such physical models, we focus on the flow resistance model in the solid-liquid coexistence zone, the so-called mushy zone. The mushy zone flow resistance model proposed by Voller and Prakash [29] has been used in a number of studies of multiphysics CFD simulation of L-PBF. The Voller-Prakash model is described as follows.

$$f_{d,i} = C\frac{\left(1-f_l\right)^2}{{f_l}^3+q}u_i, \tag{1}$$

where $f_{d,i}$, f_l, q and u_i are the fluid drag force, the volume fraction of the liquid phase, a constant to prevent division by zero and the flow velocity, respectively. The parameter C, referred to as the mushy zone constant, is assumed to be a constant determined according to the solidification morphology. The Kozeny-Carman equation [30–32], which is the basis of the Voller-Prakash model, includes morphological parameters such as the specific surface area of the porous media, the hydraulic tortuosity and the shape factor. The shape factor is a constant related to the cross-sectional shape perpendicular to the flow [30]. In Eq. (1), C combines a group of morphological parameters in the Kozeny-Carman equation into a single empirical parameter. Hence, the reduction in flow velocity due to the decrease in liquid fraction depends almost exclusively on C. Furthermore, while Eq. (1) is the relationship between drag force and liquid fraction, it should be noted that the original Kozeny-Carman equation is a linear relationship between pressure gradient and liquid fraction (porosity) in a porous medium. Even with the same porosity, the morphology of porous media can be different. A representative morphological parameter included in the Kozeny-Carman equation is the specific surface area. The pressure gradient acts on the surface area of the porous media, which means that changes in morphology could lead to variations in drag force, even for the same porosity. However, we can hardly find the studies that investigated the constant C in Eq. (1) from the perspective of morphology. Previous studies have used different values of C, such as $C = 2.5\times10^5$ for the simulation of a latent heat thermal energy storage system [33], and $C = 10^6$ [25], 5.56×10^6 [18], 10^5-10^7 [17] and 10^{14} [21] for the simulations of the L-PBF. In addition, previous studies have highlighted the influence of the mushy zone constant on melting and solidification behaviour. Shmueli et al. have reported that C significantly affects the area of the molten region inside the cylindrical tube for latent heat energy storage system (LHTES) application [34]. For L-PBF simulation, the authors of these studies have performed a series of multiphysics simulations varying C and reported that C has little effect on the dimensions of the molten pool when $P = 300$ W and $V = 1000$ mm/s for the material of Inconel738LC [28]. Wang et al. have reported that the parameter C can affect the collapse behaviour of the keyhole pore [18]. They have also reported that the value of C affects the surface velocity distribution for the keyhole mode molten pool, implying that C should affect the formation and displacement of the keyhole pores.

The mushy zone constant C is a parameter that reflects the influence of porous morphology; however, we have not found examples of previous studies that have defined C based on morphology. It is well known that dendrites form during metal solidification. The dendrites are known to develop multiple columnar structures towards the normal direction of the solid/liquid interface. This means that the value of C should be based on morphological parameters that reflect this columnar structure.

In the light of the above, the following issues need to be considered for the mushy zone constant.

- The relationship between pressure gradient and liquid fraction should be converted to a relationship between drag force and liquid fraction.
- The impact of solidification morphology should be taken into consideration.

The aim of this study is to address the aforementioned issues. A relation between drag force and liquid fraction was derived by applying the widely known fluid drag equation and Bernoulli's theorem to the Kozeny-Carman equation. The values of C were then calculated for three morphology types of solidification: (1) rectangular shape, (2) a cone, and (3) an assembly of cones, respectively. Flow resistance forces were determined for three different morphologies and compared with those calculated using the commonly used C value, as a flow Reynolds number of 1 is the limit of the Kozeny-Carman equation. Furthermore, the impact of the mushy zone constant on keyholing behaviour in L-PBF was evaluated using the multiphysics CFD simulation.

2. Kozeny-Carman-based mushy zone flow resistance model

2.1. Drag force-liquid fraction relation

The Voller-Prakash model (Eq. (1)) is based on the Kozeny-Carman equation, which represents the relationship between the porosity of the porous media and the hydraulic conductivity (k).

$$k = \frac{\rho g}{\mu}\frac{1}{\phi}\frac{1}{{S_s}^2}\frac{1}{\tau^2}\frac{\epsilon^3}{(1-\epsilon)^2}, \tag{2}$$

where k, ρ, g, μ, ϕ, S_S, τ and ϵ are the hydraulic conductivity of the porous media, the fluid density, the gravitational acceleration (9. 81 m/s^2), fluid viscosity, specific surface area (the ratio of the surface area to the volume of the porous media), hydraulic tortuosity, and porosity (determined by the ratio of pore volume to bulk volume of the porous media), respectively. The Kozeny-Carman equation is a commonly used equation for soil and rocks, with the fluid phase being water in porous media. This study specifically focuses on the melting and solidification of metallic materials, assuming that the mushy zone is represented by either solid or liquid metal. When denoting the volume fractions of the solid and liquid phases as f_s and f_l, Eq. (3) can be obtained.

$$f_s + f_l = 1. \tag{3}$$

The relationship between the pore volume (V_v), the porous volume (V_s), the bulk volume (V), and the porosity (ϵ) is as follows.

$$\frac{V_s+V_v}{V} = \frac{V_s}{V} + \epsilon = 1. \tag{4}$$

From Eqns. (3) and (4), f_l is used instead of ϵ in Eq. (2) for the purposes of this study.

Darcy's Law describes the relationship between the pressure drop due to porous flow (Δp) and the porous flow velocity (U).

$$U = k\frac{\Delta p}{\rho g L}, \tag{5}$$

where L is the length of the porous material in the direction of flow. By applying Eqns. (2) and (5), we can derive Eq. (6).

$$\frac{\Delta p}{L} = \mu\phi {S_s}^2\tau^2\frac{\left(1-f_l\right)^2}{{f_l}^3}U, \tag{6}$$

Voller and Prakash [29] formulated Eq. (1) under the assumption that the drag force is related to the pressure drop.

In this study, we introduce the following assumption (Eq. (7)) to convert Eq. (6) into the relationship between drag force and liquid fraction.

$$\Delta p = \frac{1}{2}\rho U^2. \tag{7}$$

Eq. (7) means that the static pressure is perfectly converted into the dynamic pressure. Eq. (7) is known as Bernoulli's law if the fluid is a non-viscous fluid (perfect fluid). The molten metal is a viscous fluid; however, Eq. (7) does not consider the dissipation due to viscosity. The justification of Eq. (7) for the viscous fluid will be verified by the CFD simulations in our future work.

A commonly used equation for fluid drag is as follows.

$$F_D = \frac{1}{2}\rho U^2 A C_D, \tag{8}$$

where A and C_D are the cross-sectional area perpendicular to the flow direction and the drag coefficient, respectively. Substituting Eqns. (6) and (7) into Eq. (8) gives Eq. (9).

$$F_D = \mu\phi {S_s}^2\tau^2 L A C_D\frac{\left(1-f_l\right)^2}{{f_l}^3}U. \tag{9}$$

The equation should be structured as follows: It is important that Eq. (9) includes the porous morphological parameters: τ, S_S, ϕ and A. For this study, we calculated the specific values for the morphological parameters of simple solidification geometries. Additionally, it should be noted that L, which refers to the grid size in numerical simulations, is also significant. Eq. (9) shows that the drag force is dependent on the scale, which distinguishes it from Eqns. (1) and (9).

2.2. Rectangular morphology

Fig. 1 shows an illustration of a morphology with a rectangular shape. Previous studies have observed the dendrite columnar structures. According these studies, the dendrite length is estimated to be in the range of a few hundred micrometres [35–40]. In contrast, the primary dendrite arm spacing (the distance between two dendrites) has been measured to be several micrometres [41–43]. In this study, it is assumed that dendrites begin to grow in the range of a few micrometres and extend to measured lengths of hundreds of micrometres or more. Therefore, in this section, the solidification morphology is modelled as a rectangular shape at the onset of dendrite growth.

The multiphysics CFD simulation of the L-PBF was performed using a grid resolution of several micrometres, which is significantly smaller than the several hundred micrometres dendrite structure observed in the experiment. Hence, the micrometre-grid provides only a partial surface profile of the dendrite. Using the height (h_{sol}), area (A_{sol}) and volume (V_{sol}) of the solidified metal part from Fig. 1, Eq. (10) can be used to express the specific surface area (S_S).

$$S_s = \frac{A_{sol}}{V_{sol}} = \frac{L^2}{h_{sol}L^2} = \frac{1}{h_{sol}}. \tag{10}$$

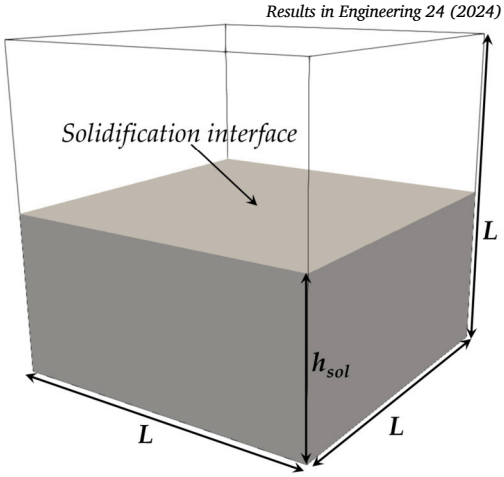

Fig. 1. A rectangular-shaped solidification morphology.

The drag coefficient (C_D) is influenced by both the shape of the object and the Reynolds number (Re) of the fluid. The Kozeny-Carman equation is applicable for low Re flow regimes [44–46]. For the flow through porous media, the Re is typically between 1 and 10 [44]. In this study we have assumed Re = 1 to satisfy the constraints of the Kozeny-Carman equation. Note that Re = UD/μ, where D is the characteristic length, for example, the average particle size is often used as D for granular material. In this study we have chosen to use the grid size L as for D. By setting L to 2.5 μm, the velocity U is about 0.14 m/s to obtain Re = 1. It is worth noting that the grid size of 2.5 μm was previously implemented in our multiphysics CFD simulations [47]. It is widely recognised that C_D depends on the Re. In the low Re flow regime, specifically characterised by laminar flow, the C_D of a sphere is obtained by calculating 24/Re. According to Stokes' law, we have C_D = 24 when Re = 1. According to a previous study using two-dimensional CFD simulation [48], it was found that the C_D of a square is greater than that of a circular shape, with the respective C_Ds being 11.72 and 12.9. In addition, the C_D of a disc and a plate are of the order of Re = $O(10^1)$ [49]. Therefore a value of C_D = 10 was used in this study.

The τ characterises the degree of twisting of the streamlines. In Fig. 1, τ = 1 because there is no flow twisting in the direction parallel to the solidification interface (grey in Fig. 1). The flow is stopped by the solidification interface in the direction perpendicular to the interface. Hence, we choose τ = 1 for Fig. 1.

The A is equal to L^2 for the direction perpendicular to the solidification interface, but the flow along this direction is impeded by the interface. For the direction parallel to the interface, $A = h_{sol}L$. The μ denotes the viscosity of the molten metal, which in this study has a fixed value of 0.005 Pas.

The determination of ϕ is theoretically difficult; therefore, the first author of this study and co-authors determined the ϕ value by back-calculation with Eq. (2) using the hydraulic conductivity (k) measured by the CFD simulations [50,51]. Unfortunately, the investigation of the ϕ value for metallic materials can not be found in the literature. Therefore, we set ϕ = 1, which means that the effect of ϕ is not considered in this study. To quantitatively determine the shape factor, we plan to obtain 3D dendrite structures by x-ray CT and perform CFD simulation using the 3D dendrite structure in our future work.

The liquid fraction, denoted f_l, can be expressed by Eq. (11) as shown in Fig. 1.

$$f_l = 1 - \frac{h_{sol}}{L}. \tag{11}$$

Substituting τ = 1, ϕ = 1, μ = 0.005 Pas, $A = h_{sol}L$, and Eqns. (10) and (11) into Eq. (9), we obtained the drag force-liquid fraction relationship for Fig. 1.

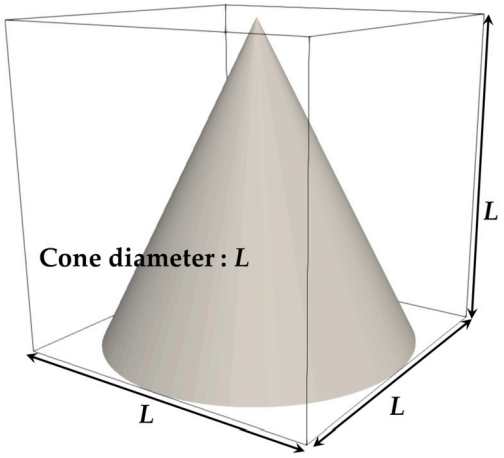

Fig. 2. A cone-shaped solidification morphology.

$$F_D = 0.1L\frac{(1-f_l)}{{f_l}^3}U, \tag{12}$$

2.3. Conical morphology

Fig. 2 displays a conical-shaped morphology. The model assumes a single dendrite tip grows within a single grid, meaning no multiple micro-cones exist in the grid. Eq. (13) calculates the S_S for the geometry presented in Fig. 2.

$$S_s = \frac{A_{sol}}{V_{sol}} = \frac{\frac{\sqrt{5}\pi L^2}{4}}{\frac{\pi L^2}{12}} = 3\sqrt{5}. \tag{13}$$

In the cone morphology, the flow field varies in different directions: left-right (and front-back) and top-bottom. The τ has a value of approximately one at the top of the cone in the left-right direction. In contrast, at the bottom of the cone, the streamline is half the circumference of the cone base, giving $\tau = \pi L/L$. Assuming that a representative τ for the left-right direction is at the centre of the cone height, then $\tau = (\pi+1)/2$. The A for the left-right direction equals $L^2/2$. For the top-bottom direction of Fig. 2, the streamlines assume to be straight along the ridge of the triangle (projection view from the side of the cone); as a result, $\tau = \sqrt{3/2}$. The A for the top-bottom direction is the circle's area (the cone's base), with a value of $\pi L^2/4$.

We presumed to $C_D = 10$ for both the left-right and top-bottom directions although the A is different for the left-right and top-bottom directions. In both of the left-right and top-bottom directions, ϕ is assumed to be 1. Eqns. (9), (14) and (15) can be derived for the left-right and top-bottom directions by incorporating the aforementioned morphological parameters.

$$F_D = 4.82L^3\frac{(1-f_l)^2}{{f_l}^3}U, \tag{14}$$

$$F_D = 2.65L^3\frac{(1-f_l)^2}{{f_l}^3}U. \tag{15}$$

According to Eqns. (14) and (15), the difference in F_D values between the left-right and top-bottom directions is insignificant. The key implication of Eqns. (14) and (15) is that the F_D is contingent on L^3, which becomes significantly smaller when the grid size is a few micrometres.

2.4. Cone assembly

In this section, we consider a geometry composed of multiple dendrite columns. Fig. 3 displays that the cone assembly morphology, i.e., cones are regularly arranged on the bottom plane. n cones are aligned along one direction of the parallel to the bottom plane; as a result, a total of n^2 cones are placed in the grid. Fig. 3 is an example for $n = 5$. To calculate S_S for cone assembly composed of n cones, we use Eq. (16).

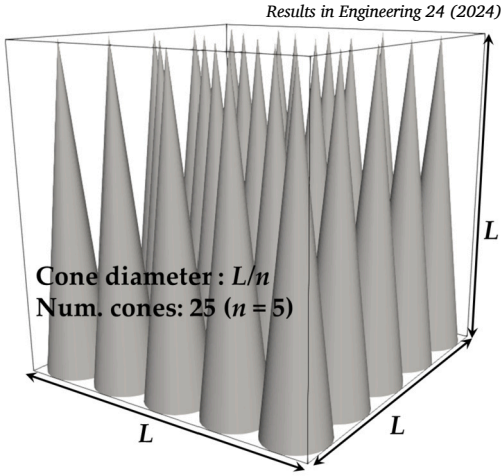

Fig. 3. An example of solidification morphology composed of cone assembly: 25 cones ($n = 5$).

$$S_S = \frac{A_{sol}}{V_{sol}} = \frac{\left(\frac{n\pi L^2}{2}\sqrt{1+\frac{1}{4n^2}}\right)}{\frac{\pi L^2}{12}} = 6n\sqrt{1+\frac{1}{4n^2}}, \tag{16}$$

For the left-right direction, the value of τ is expressed by Eq. (17), assuming that the streamline length at the centre of the cone height represents the average of the entire geometry.

$$\tau = \frac{1}{4}\left((1+\pi)+\frac{1}{n}\right)(\text{for } n>1). \tag{17}$$

Moreover, the A is a collection of n triangles; hence $L^2/2$.

For the top-bottom direction, $\tau = \sqrt{1+1/4n^2}$ which is the ridge length of one of the triangles. The A is $\pi L^2/4$, which is the area of a group of n^2 circles.

For the both left-right and top-bottom directions, the values of ϕ and the C_D are set to 1 and 10, respectively. The C_D in the left-right as well as in the top-bottom directions are expressed in Eqns. (18) and (19), respectively.

$$F_D = 0.90n^2\left(\frac{(1+\pi)n+1}{4n}\right)^2\left(1-\frac{1}{4n^2}\right)L^3\frac{(1-f_l)^2}{{f_l}^3}U, \tag{18}$$

$$F_D = 1.41n^2\left(1-\frac{1}{4n^2}\right)^2 L^3\frac{(1-f_l)^2}{{f_l}^3}U. \tag{19}$$

3. Results and discussions

3.1. Comparison of drag force

Table 1 shows the constant values of the mushy zone constant used in past studies. The abbreviation LHTES in Table 1 denotes Latent Heat Thermal Energy Systems.

The micrometre grid was used in the multiphysics CFD simulations in the past studies, as listed in Table 1. Despite the grid size, these studies used a mushy zone constant greater than 10^5. Our calculations of the F_D values were carried out on a 2.5 μm grid size, with $U = 0.14$ m/s to achieve Re $= 1$, and n in Eqns. (18) and (19) set to 5. Fig. 4 shows the relationship between F_D and f_l using the Voller-Prakash model with the use of $C = 10^6$ (equation (1)), alongside Eqns. (12), (14) and (15), in addition to Eqns. (18) and (19), when $n = 5$.

Table 1
Mushy zone constant (C in Eq. (1)) used in the past studies.

C [kg/(m^3s)]	Grid size	Phenomenon
1.6×10^5	1/80 lattice unit	Thermal cavity [29]
2.5×10^5	≈1.81 mm	LHTES [33]
10^5-10^7	4 μm	L-PBF [17]
10^5-10^{10}	≈0.5 mm	LHTES [34]
1×10^8	2×2×1 μm^3	L-PBF [22]
5.56×10^6	4 μm	L-PBF [18]
1×10^6	5 μm	L-PBF [25]
1×10^{14}	4 μm	L-PBF [21]

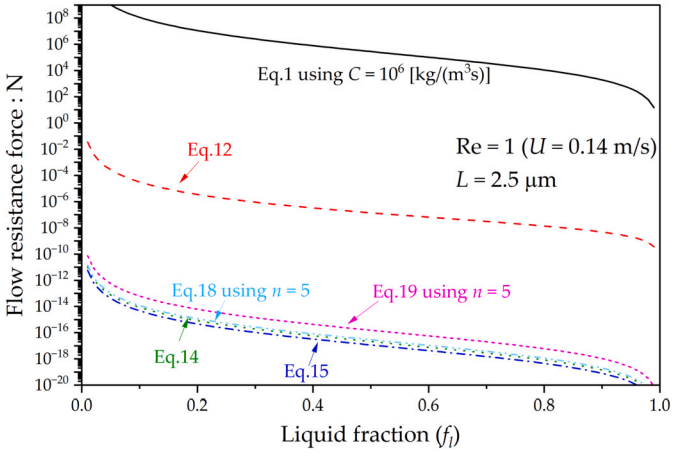

Fig. 4. Relationship between liquid fraction (f_l) and drag force (F_D) calculated by the Voller-Prakash model and proposed models in this study.

The drag force calculated from the proposed models in this study, represented by Eqns. (12), (14), (15), (18) and (19), are significantly lower than that of the Voller-Prakash model. This is due to the dependence of the proposed models on the grid size (L). In particular, Eqns. (14), (15), (18) and (19) have an influence on F_D of the order of L^3; hence their F_D values are significantly smaller than those of Eq. (1).

The large C value has been used in most of the past studies. Li et al. have performed the multi-physics simulation with different C values. They have reported the C influenced the velocity fields inside the molten pool and the surface shape of the top of the molten pool [52]. In their study, the molten pool shape predicted from the simulation is reasonably agreed with that of the experimental observation.

The authors of this study have confirmed that C has little effect on the molten pool shape predicted by the simulation [47]. The mushy zone is a region whose temperature is between the liquidus and solidus temperatures and can occur in two phases: the melting (heating) phase and the solidification (cooling) phase. In the melting phase, the powder bed and substrate are rapidly melted and depressed by evaporation. During the vapor depression, the temperature of the vaporised gas rises rapidly and reaches more than 4,000 K [47]. The mushy zone occurs slightly inside the depressed metal surface. The high gas temperature results in a large spatial temperature gradient towards the interior of the metal. The spatial gradient between the solidus and liquidus temperatures will be confined to a narrow region. The molten pool is the maximum area melted by the laser irradiation. Therefore, the mushy zone constant has little effect on the molten pool dimensions because the mushy zone is confined to a very small area in the melting phase.

In contrast, the mushy zone of the solidification process will continue for a longer period of time than that of the melting phase, i.e., the dynamic and drastic process caused by the laser irradiation. As a result, the length of the molten pool along the direction of laser movement will be influenced by the mushy zone constant. Wang et al. have investigated the influence of the mushy zone constant on the keyhole behaviour and

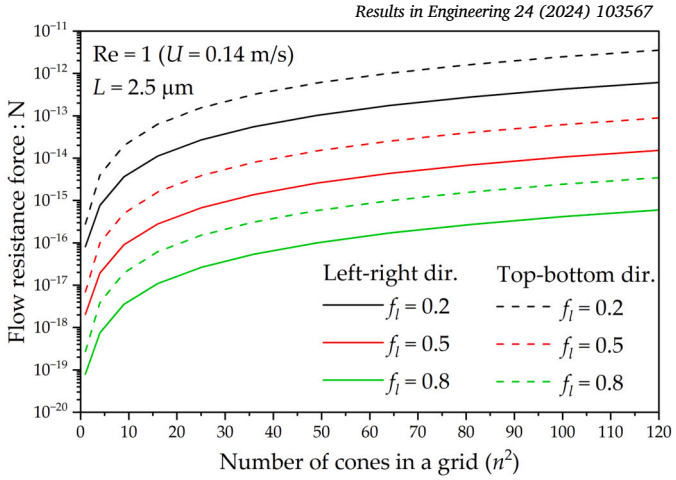

Fig. 5. Relationship between number of cones (n^2) and drag force calculated by Eqns. (18) and (19).

reported that the mushy zone constant affects the velocity distribution of the keyhole type molten pool [18], which suggests that the mushy zone constant can influence keyhole pore formation and its dynamics.

3.2. Solidification morphology effect

Equations (18) and (19) enable us to assess the effect of the number of cones (n) on F_D. Fig. 5 illustrates the effect of n on F_D for f_l values of 0.2, 0.5 and 0.8. Note that Eqns. (18) and (19) have been calculated using a value of $U = 0.14$ m/s and $L = 2.5$ μm.

As the n increases, the F_D tends to increase monotonically; the increase in F_D becomes moderate as n increases. The S_S strongly influences the change of the increasing trend. Eq. (9) proves that μ, ϕ, L and C_D are identical regardless of n: the two factors: τ and S_S can modify F_D.

When $n = 2$, the τ of the cone assembly for the left-right direction is about 2.20. The τ of the conical assemblies for the top-bottom direction is $\sqrt{1.25}$ when $n = 1$. These τ values do not have a strong effect on F_D. The previous studies have demonstrated that τ cannot take a large value for dense packing of granular materials and rock. The morphological parameters in the Kozeny-Carman equation obtained in the past studies and the C values estimated from such morphological parameters in the past studies are summarised in Table 2. The sandstone formed by consolidation and particle crushing under high effective stress conditions in the deep subsurface has $\tau = 3.1$ for the porosity of 0.25 [53]. Unlike τ, the S_S is the same for the left-right and top-bottom directions. In addition, S_S is not a dimensionless parameter, which means that the S_S value varies significantly depending on the microstructural morphology and should be a highly influential factor for F_D. Note that A is the projected cross-sectional area, which is different from the surface area used to calculate S_S. That is, the surface area is the total area of the solid surface in contact with the liquid surface. It is reasonable from a physical point of view that the greater the surface area, i.e. the more complex the morphology, the greater the drag force.

3.3. Revisit on mushy zone constant

As shown in Table 1, different values of C have been used in past studies, mostly greater than 10^5. As described in the introduction, the single parameter C in Eq. (1) has been derived from a set of morphological parameters of the Kozeny-Carman equation. In this study, we have derived the novel fluid drag-liquid fraction relationship (Eq. (9)) in order to keep the morphological parameters of the Kozeny-Carman equation. Prior to the discussion, we will exclude L and A in Eq. (9) because they are grid-dependent parameters. The C values were calculated using the measured values of ϕ, τ and S_S: $C = \phi\tau^2 {S_S}^2$.

Table 2
The mushy zone constant values estimated from the past studies.

Material	ϵ	ϕ	τ	S_S [m^{-1}]	C [kg/(m^3s)]	Ref.
Cylinder	-	2.5	$\sqrt{2}$	$4/D$	$80/D^2$	[30,31]
Spheres	-	2.5	$\sqrt{2}$	$6/D$	$180/D^2$	[30,31]
Al-Cu alloy	≈0.25	-	-	1.35×10^5	$1.82\times10^{10}\phi\tau^2$	[54]
Zinc battery	-	-	-	1.04×10^6	$1.08\times10^{12}\phi\tau^2$	[55]
Al-15.5%Cu alloy	-	-	-	1.62×10^5	$2.62\times10^{10}\phi\tau^2$	[56]
Al-19.5%Cu alloy	-	-	-	1.08×10^5	$1.17\times10^{10}\phi\tau^2$	[56]
Ni-Al-W alloy (C)	0.1	-	1.30	1.86×10^5	$5.85\times10^{10}\phi$	[57]
Ni-Al-W alloy (C)	0.2	-	1.18	4.94×10^5	$3.40\times10^{11}\phi$	[57]
Ni-Al-W alloy (C)	0.3	-	1.16	5.75×10^5	$4.45\times10^{11}\phi$	[57]
Ni-Al-W alloy (C)	0.4	-	1.25	4.74×10^5	$3.51\times10^{11}\phi$	[57]
Ni-Al-W alloy (C)	0.5	-	1.19	2.05×10^5	$5.95\times10^{10}\phi$	[57]
Ni-Al-W alloy (C)	0.6	-	1.24	7.37×10^4	$8.35\times10^9\phi$	[57]
Ni-Al-W alloy (C)	0.6	-	1.27	3.73×10^4	$2.24\times10^9\phi$	[57]
Ni-Al-W alloy (P)	0.25	-	1.51	2.63×10^5	$1.58\times10^{11}\phi$	[57]
Ni-Al-W alloy (P)	0.35	-	1.19	8.90×10^5	$1.12\times10^{12}\phi$	[57]
Ni-Al-W alloy (P)	0.45	-	1.32	6.62×10^5	$7.64\times10^{11}\phi$	[57]
Ni-Al-W alloy (P)	0.55	-	1.24	4.18×10^5	$2.69\times10^{11}\phi$	[57]
Ni-Al-W alloy (P)	0.65	-	1.10	1.67×10^5	$3.37\times10^{10}\phi$	[57]
Ni-Al-W alloy (P)	0.75	-	1.24	4.41×10^4	$2.99\times10^9\phi$	[57]
Ni-Al-W alloy (P)	0.85	-	1.07	3.55×10^4	$1.44\times10^9\phi$	[57]
Glass beads	0.33	4.60	1.31	3.69×10^4	1.07×10^{10}	[50]
Glass beads	0.37	5.90	1.26	4.15×10^4	1.61×10^{10}	[50]
Glass beads	0.40	8.60	1.24	4.22×10^4	2.35×10^{10}	[50]
Fine sand	0.39	6.17	1.29	5.48×10^4	2.99×10^{10}	[50]
Fine sand	0.40	7.08	1.29	5.27×10^4	3.27×10^{10}	[50]
Fine sand	0.42	9.35	1.28	5.33×10^4	4.35×10^{10}	[50]
Cylinders (C)	0.223	0.60	1.03	1.63×10^4	1.69×10^8	[51]
Spheres	0.472	1.90	1.21	1.89×10^4	9.94×10^8	[51]
Sandpack LV60A	0.38	-	-	2.21×10^4	3.54×10^9	[53]
Sandpack F62A	0.33	-	-	1.47×10^4	1.29×10^9	[53]
Sandstone	0.25	-	-	2.73×10^4	9.09×10^9	[53]

Carman, who proposed the Kozeny-Carman equation [30,31], suggested that $\tau = \sqrt{2}$ and $\phi = 2.5$ from the geometrical consideration for a regular array of monodisperse spheres [30]. He also proposed S_S as $4/D$ and $6/D$ for monodisperse cylinders and spheres respectively. Note that D is the diameter of the cylinder or sphere. As a result, C for the monodisperse cylinders and spheres are $80/D^2$ and $180/D^2$ respectively. It is important to note that C values estimated using Carman's morphological parameters include the factor $1/D^2$. As the D becomes smaller, the C increase in the order of D^2.

For the real metallic materials, the value of S_S has been determined by x-ray CT. The values of S_S obtained from x-ray CT images are listed in Table 2 and range between 10^4 and 10^6 m^{-1}, although the materials have been varied in the literature. From Eq. (9), the drag force depends on the square of S_S. The factor $\phi\tau^2$ is assumed to be greater than 1; as a result, the value of C will be in the order of 10^{10} and 10^{12}. Madison et al. have performed flow simulations using the 3D columnar structures obtained from x-ray CT as boundary conditions and directly evaluated τ [57]. According to their simulations, τ differs between flow parallel and perpendicular to the dendrite growth direction. The term "(C)" in Table 2 refers to the direction perpendicular to the dendrite growth, while the term "(P)" refers to the same direction as the dendrite growth. Madison et al. have found that the difference in τ due to flow direction is insignificant, implying that C is insignificantly affected by flow direction. In the model derived in this study, there is an insignificant difference in the C values between the left-right and top-bottom directions, which follows the findings of Madison et al.

Table 2 contains data obtained from x-ray CT analysis and flow simulation using the 3D porous structure of the granular material and rock. Although the morphology of the dendrite columnar structure and that of the granular material and rock are clearly different, the values of τ and S_S are found to be similar, which suggest that their C values is also similar.

To the best of the authors' knowledge, there is no direct method to determine the shape factor ϕ; therefore, the first author of this study and co-authors have estimated the ϕ value by back-calculation using the hydraulic conductivity, τ, S_S and ϵ calculated by the flow simulation [51,50]. The ϕ values estimated by the back-calculation are listed in the Table 2 and are of the order of $O(10^0)$. In the case of glass beads and fine sand, C is found to be of the order of $O(10^{10})$. In the case of dendrite structures of alloy, Madison et al. [57] did not provide the values of ϕ. Assuming that $\phi = 10$ is applied to the dendrite structure, the C values are expected to be in the order of $O(10^{10})$ to $O(10^{12})$. Furthermore, τ^2 is estimated to be at most 1.5 in the CFD simulation of Madison et al. [57]. Assuming that $\tau = 1.5$ and ϕ is 10, $\phi\tau^2 \approx 22.5$; as a result, the C values for the other alloys [54,56] are of the order of $O(10^{11})$. These results suggest that the large C values used in previous studies are reasonable.

However, there is actually the characteristic length for the alloy dendrite structure; therefore, the solidification morphology should be varied depending on the characteristic length, i.e., the grid size of the simulation. Several previous studies have reported that the scale of the dendrite is estimated to be between several hundred μm to several mm, for example, [35–40]. In contrast, several micrometre grid has been used in most of previous studies for the multiphysics CFD simulation, see., Table 1. As shown in Table 1, Voller and Prakash have proposed the C value of Eq. (1) for relatively large grid sizes. When the grid size is significantly larger than the scale of the dendrites, it is reasonable to apply the commonly used C values: between 10^5 and 10^7. However, due to the characteristic length scale in the dendrite formation mechanism, complex morphologies, such as cone assembly are difficult to form in several micrometre grids, as in the studies listed in Table 1 and the present study. For the simulation using several micrometre grid, the rectangular morphology could be reasonable among the models proposed in this study.

4. Influence of mushy zone constant on keyholing behaviour

4.1. Simulation overview

To validate the proposed models, the keyhole pore formation simulation was carried out following Wang et al. [18]. The simulation includes

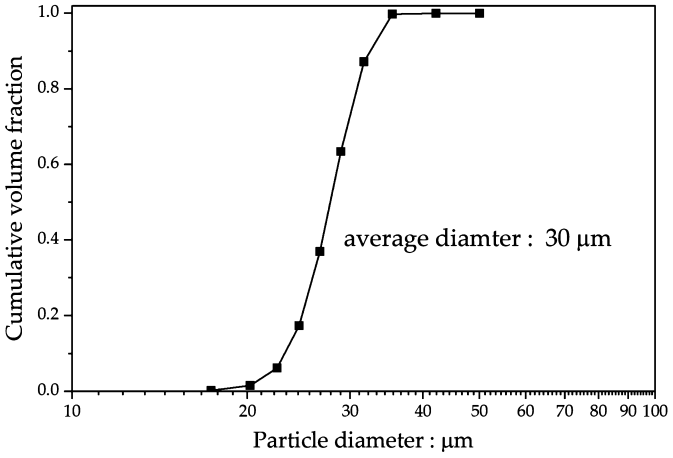

Fig. 6. Particle size distribution of the powder.

multiphysics of the L-PBF such as solid-liquid-vapour phase change and its multiphase flow, heat conduction with the vaporisation-melting-solidification, laser heating by ray tracing. In addition, the simulation with the powder bed generated by the discrete element method (DEM) simulation. A brief summary of the simulation procedure is given in this paper; the full simulation methodology and validation through systematic comparison with the experiments can be described in detail in our previous publications [47,58].

4.1.1. Discrete-element modelling of powder spreading

We used the general purpose DEM software: LIGGGHTS (version 3.8.0) in this study. The particle size distribution shown in Fig. 6 were used in the DEM simulation. The Young's modulus and Poisson's ratio of the particles were set to 5×10^6 N/m and 0.4, respectively. Both the particle-particle and the particle-wall friction coefficients were set to 0.3. The "f" style boundary condition was adopted in this study. The "f" boundary acts as a fixed smoothed wall boundary, but the particles are removed when the particles fall outside the domain. Note that it is difficult to completely reproduce the behaviour of physical phenomena in physical simulations; therefore, certain assumptions are often incorporated. For example, a homogeneity, an isotropy, and a linear elasticity have been employed in the mechanical simulation of elastic bodies [59–62]. In the context of the DEM, the particles, which would ideally be modelled as elastic bodies, are instead assumed to be rigid particles. The two elastic particles undergo deformation when in contact with one another. The elastic particles in contact are simulated by allowing for slight overlap of the rigid particles in the DEM. In the case of a low contact force, the deformation of elastic particles in contact is small. In this case, the rigid-body assumption is reasonable. In the DEM, the overlap distance between the particles mainly depends on the time increment and the particle contact stiffness (Young's modulus). In this study, the time increment of 2×10^{-8} sec was identified by a parametric study, as it ensures that the overlap between the particles remains within acceptable distance.

The width (x), depth (y), and height (z) of the DEM model domain are 6.2 mm, 2 mm, and 0.75 mm. The 80,000 powder particles were randomly generated to a rectangular region above a powder coating space which was a concave and rectangular space on top of the DEM model. The width, depth, and height of the powder coating stage were 4.5 mm, 1.5 mm, and 0.08 mm, respectively. Then, the powder particles were settled under the gravity. After the gravitational deposition, a rectangular-shaped coating blade moves toward x-direction with 25 mm/s speed to spread the powder particles within the powder coating space. A snapshot during powder spreading simulation is shown in Fig. 7.

4.1.2. Governing equation of multiphysics CFD simulation

The positions and radii of the powder particles were used as the initial conditions for the multiphysics CFD simulation. We used the multiphysics CFD solver based on OpenFOAM-8, which was partly developed by TERRABYTE Co. Ltd, Tokyo, Japan.

In the multiphysics CFD simulation, both gas and liquid (solid and liquid metal) are assumed to be incompressible fluids. The interface between solid or metal (phase 1) and gas (phase 2) is captured by the function F using the Volume of Fluid (VOF) method.

$$\frac{\partial F}{\partial t}+\frac{\partial F u_j}{\partial x_j}=0, \tag{20}$$

where, F is the value of the VOF function ($0\leq F\leq1$). The time evolution of the interface is calculated by solving the advection equation of F.

The governing equations used in the simulations are the energy equation, the continuity equation and the conservation of momentum, which are expressed in Eqns. (21), (22) and (23) respectively.

$$\frac{\partial(\rho C_p T)}{\partial t}+\frac{\partial(\rho u_j C_p T)}{\partial x_j}=-\frac{\partial q_j}{\partial x_j}+\dot{q_m}+\dot{q_v}, \tag{21}$$

$$\frac{\partial u_i}{\partial x_i}=0, \tag{22}$$

$$\frac{\partial(\rho u_i)}{\partial t}+\frac{\partial(\rho u_i u_j)}{\partial x_i}=-g_j\left(x_j-r_j\right)\frac{\partial\rho}{\partial x_i}+\frac{\partial}{\partial x_j}\left\{\mu\left(\frac{\partial u_i}{\partial x_j}+\frac{\partial u_j}{\partial x_i}\right)\right\}+F_{CSF,i}+F_{r,i}+S_i, \tag{23}$$

where ρ, C_p, u_i, r_j, q_j, μ, $\dot{q_m}$ and $\dot{q_v}$ are the density, specific heat capacity, flow velocity, reference point, heat flux, viscosity, phase change heat dissipation term and phase change heat absorption term, respectively. Eqns (21), (22) and (23) are solved using the Finite Volume Method (FVM). In the FVM algorithm, a computational domain is partitioned by a set of polyhedral volume elements: control volumes. The governing equations are discretised to algebraic equations that are conservative for each control volume. The FVM in OpenFOAM is described in detail in the cited references [63–66]. The FVM has been a standard tool for CFD in both academic and industrial engineering for many years. The FVM is distinguished by its simplicity of algorithmic structure and robustness. Furthermore, the FEM is frequently employed for CFD. However, the FEM is applicable to a variety of physical phenomena described by partial differential equations, including thermal fluid behaviour of the L-PBF [20] and the mechanical behaviour of materials [67–71]. In the manufacturing process of L-PBF, the thermal fluid behaviour is of great importance. However, warping (plastic deformation) due to the residual stress cannot be evaluated by the FVM. In order to evaluate such phenomena, it is necessary to simulate thermo-elastoplastic behaviour. The FEM is suitable for performing simulations of both thermal fluid behaviour analysis and thermo-elastoplastic analysis.

The terms $F_{\mathrm{CSF},i}$, $F_{r,i}$ and S_i are the surface tension term using the continuum surface force (CSF) model, the recoil pressure and the mushy zone flow resistance force, respectively. The surface tension, recoil pressure and mushy zone flow resistance models are expressed in the Eqns. (24), (25) and (26) respectively.

$$F_{CSF,i}=\sigma\kappa\frac{\partial F}{\partial x_i}, \tag{24}$$

$$F_{r,i}=-0.54P_0\exp(\left(L_v\frac{T-T_v}{RTT_v}\right))\mathbf{n}, \tag{25}$$

$$S_i=-C\frac{\left(1-f_l\right)^2}{{f_l}^3}u_i, \tag{26}$$

where σ, κ, P_0, L_v, R, T_v, and $\mathbf{n}$ are the surface tension coefficient, the curvature of the gas-liquid interface, the gas phase pressure, the latent heat of evaporation, the gas constant, the evaporation temperature, and a unit normal vector of the gas-liquid interface, respectively.

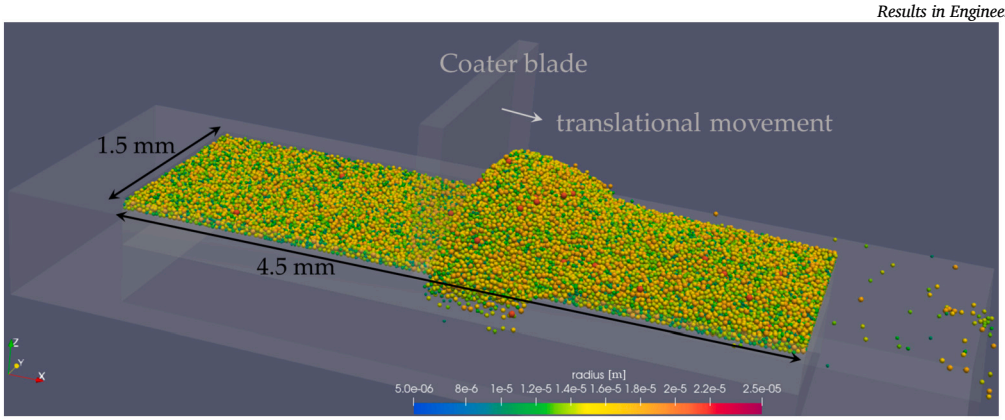

Fig. 7. A snapshot of powder spreading DEM simulation.

The ray tracing algorithm treats the laser beam as a bundle of laser beams and tracks each beam. Thermal energy is applied to the metal surface when the beam reaches the surface and is calculated from a laser reflectivity (absorptivity) of the metal surface. The laser rays repeat the mirror reflections until the applied thermal energy becomes extremely small or the laser ray does not reach the surface.

In physical simulations, it is of great importance to validate the accuracy of the simulations by assessing the fidelity with which they reproduce real-world processes. For example, in simulations of elastic materials, it is essential to determine a boundary condition that is based on an actual physical process. The resulting strains or stresses should be compared with experimental data or real-world observations [72–76]. In our previous studies, we conducted a quantitative comparison between the molten pool dimensions obtained from simulations and those obtained from experiments [47,58]. These studies have demonstrated that the molten pool dimensions obtained from the simulations were influenced by a number of factors, including vaporisation-induced recoil pressure and the laser reflectivity models used and their respective values. Note that the impact of the laser reflectivity on the molten pool dimensions is significant [47]. In the case without powder bed, it has been confirmed that the constant reflectivity value of 0.2 accurately reproduces the molten pool dimensions observed in experiments [58]. For this reason, the constant laser reflectivity value of 0.2 has also been adopted in this study.

We focused on the rectangular region within the powder-coated space, whose width and depth were 1.5 mm and 0.3 mm respectively. The upper and lower regions of the powder bed were added to form gas phase and substrate regions, respectively. The resulting CFD model domain was 1.5 mm wide, 0.3 mm deep and 0.4 mm high. The entire model domain was partitioned into 5 μm and then the inner region of 1.4 mm width, 0.2 mm depth and 0.31 mm height was partitioned into 2.5 μm grid to ensure calculation accuracy.

A constant temperature of 298.15 K was applied to the top x-y plane, and an adiabatic condition was applied to the other five planes for the thermal boundary conditions. An atmospheric pressure (101,325 Pa) was adopted for the upper x-y plane, and a zero-gradient condition was adopted for the other five sides for the pressure boundary conditions. For the flow velocity boundary conditions, the *pressureInletOutletVelocity* boundary condition implemented in OpenFOAM was adopted for the upper x-y plane. The *pressureInletOutletVelocity* condition assumed a zero gradient condition when the flow is outward direction. When the inward flow, the velocity is obtained from the flow with the specified inlet direction. The zero-gradient condition was applied to the other five sides. These boundary conditions were set based on past studies; however, they do not entirely reflect the actual conditions that would occur in a real-world setting. For Example, the effect of a vapor plume has not been incorporated in this study. The vapor plume is the metal vapor generated by laser irradiation. According to previous study, the metal vapor forms like a cloud and can reach temperatures about 5500 K [77].

Table 3
Materials properties of Inconel738LC and the simulation parameters used in this study.

Property or Parameter	Value [Unit]
Density of solid	8820 [kg/m^3]
Density of liquid	8220 [kg/m^3]
Density of gas	1.176 [kg/m^3]
Solidus temperature	1371.15 [K]
Liquidus temperature	1620.15 [K]
Evaporation temperature	3034.0 [K]
Thermal conductivity	46.1 [W/(m·K)]
Latent heat of fusion	25,000 [J/kg]
Latent heat of evaporation	734,000 [J/kg]
Specific heat capacity of metal	710 [J/kg·K]
Specific heat capacity of gas	1007 [J/kg·K]
Surface tension coefficient (σ)	1.2 [N/m]
Liquid viscosity (μ)	0.005 [Pa·s]
Gas viscosity	1.865×10^{-5} [Pa·s]
Liquid-gas heat transfer coefficient	40 [W/(m^2·K)]
Emissivity of thermal radiation	0.3 [-]
Laser diameter	80.0×10^{-6} [m]
Value of C in Eq. (26)	10^{-6},10^{0},10^{12},10^{18} [kg/(m^{3}s)]

Such high-temperature metal vapor may result in secondary heating the powder bed and the substrate. Indeed, our experiments revealed that the molten pool width near the top (i.e., near the substrate) was observed to be greater than that observed at the bottom or middle, for example, [28]. In the simulation, the upper thermal boundary condition along z direction is maintained at 298.15 K, which results in the continuous cooling of the molten metal. Consequently, the molten pool width near the substrate may be narrower than that at the middle region. To accurately reproduce the molten pool shape observed in the experiments, it may be necessary to incorporate the heating effect by the vapor plume into the boundary conditions.

The laser energy distribution is a Gaussian distribution and its standard deviation is set to 1.0. The laser power and scanning speed were set to 300 W and 500 mm/s respectively. The laser was initially positioned at $x = 2.7$ mm, $y = 1.0$ mm, and $z = 0.1$ mm, respectively, and then displaced horizontally toward the x direction by 1.3 mm for 2.6×10^{-3} sec. Then the laser was stopped and the spontaneous cooling simulation was performed for 0.65 sec. The computation time of the typical simulation case was about 7 days using a 96-core parallel computer. The value of C was varied by 10^{-6}, 10^{0}, 10^{6}, 10^{12} and 10^{18}. As in the previous study [47], we used the physical properties of Inconel738LC obtained using thermodynamics software: JMatPro. The physical properties and calculation parameters are listed in Table 3. Fig. 8 shows snapshots during the simulation with $C = 10^6$. The laser process parameter condition of 300 W and 500 mm/s results deep vapour depression. The tip of the vapour depression then splits and is trapped inside the substrate, which is a typical keyhole pore formation behaviour confirmed in the previous study, e.g. [78].

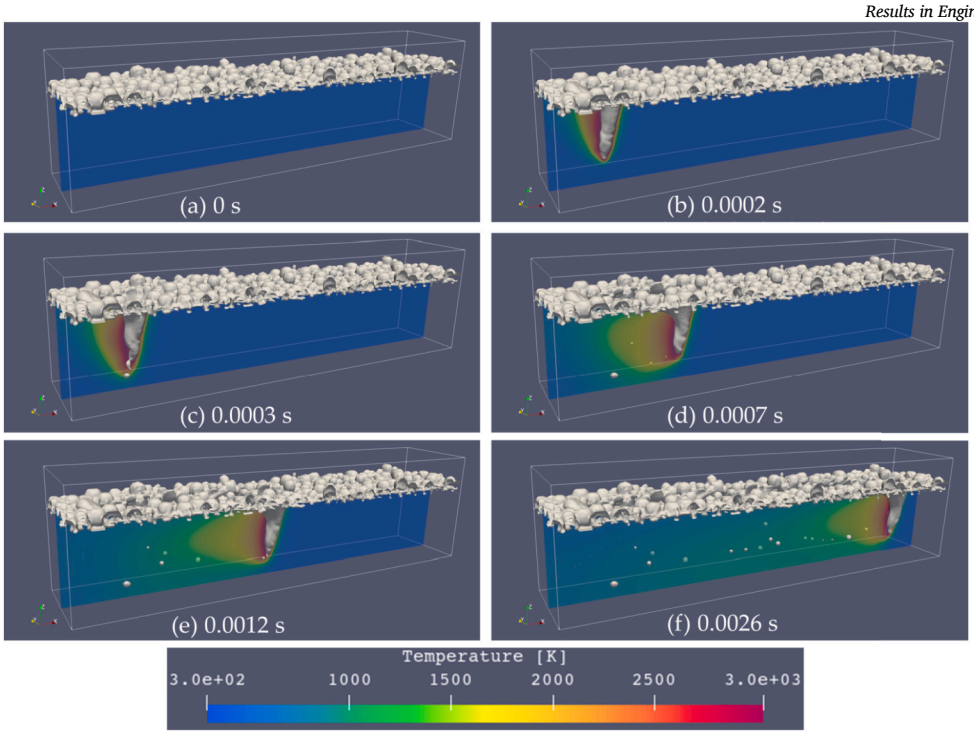

Fig. 8. Snapshots during the simulation for $C = 10^6$ kg/(m^{3}s).

4.2. Results and discussions

As a result of the simulations, we confirmed that the number, size and position of the pores were different when just the C value was varied. Therefore, we evaluated the position and size of each individual pore. We used the visualisation software Paraview (ver. 5.10.1) to generate a bounding box for each pore and measured its length along the x, y and z axes. We calculated the pore size (L_{pore}) using the following formula

$$L_{pore} = \frac{l_{bx} + l_{by} + l_{bz}}{3}, \tag{27}$$

where l_{bx}, l_{by} and l_{bz} are the bounding box lengths along the x, y and z directions respectively. Note that the bounding box is centred at $(l_{bx}/2, l_{by}/2, l_{bz}/2)$. We have calculated the positions and sizes of all the pores. The average values and standard deviations are shown in Fig. 9.

There is no correlation between the position of the y axis and C, nor between the position of the z axis and C. However, there is a correlation between the position of the x axis (along the direction of the laser scan) and C. Fig. 10 shows the velocity vectors in the x-z cross section at $y = 0.15$ mm for the simulation with $C = 10^{-6}$ and 10^{18}. The two solid lines in the figure represent the contours of the liquidus and solidus temperatures respectively. The area between the two contours is the mushy zone. The direction of flow in both the molten pool and the mushy zone is in the negative x direction; hence the pore displaces in the opposite direction to the laser scan. The use of a large value of C results in strong flow resistance on the melt, which significantly restricts pore displacement in the mushy zone. As a result, the position of the pore along the x axis is smaller when the smaller C value is used.

The pore size becomes slightly smaller with increasing C and is almost the same for $C \geq 10^6$. The standard deviations of the pore size are larger for $C \geq 10^0$ than for $C < 10^0$. As shown in Fig. 10, the flow velocity distribution in the mushy zone is very small when C is large, which means that the mushy zone can be considered almost solid. In other words, the length of the molten pool varies as C increases. Huang et al. visualised the pore formation and its dynamics during the L-PBF experiment using synchrotron x-ray CT [79]. According to them, the pores pinched off from the tips of the keyhole grow rapidly. Huang et

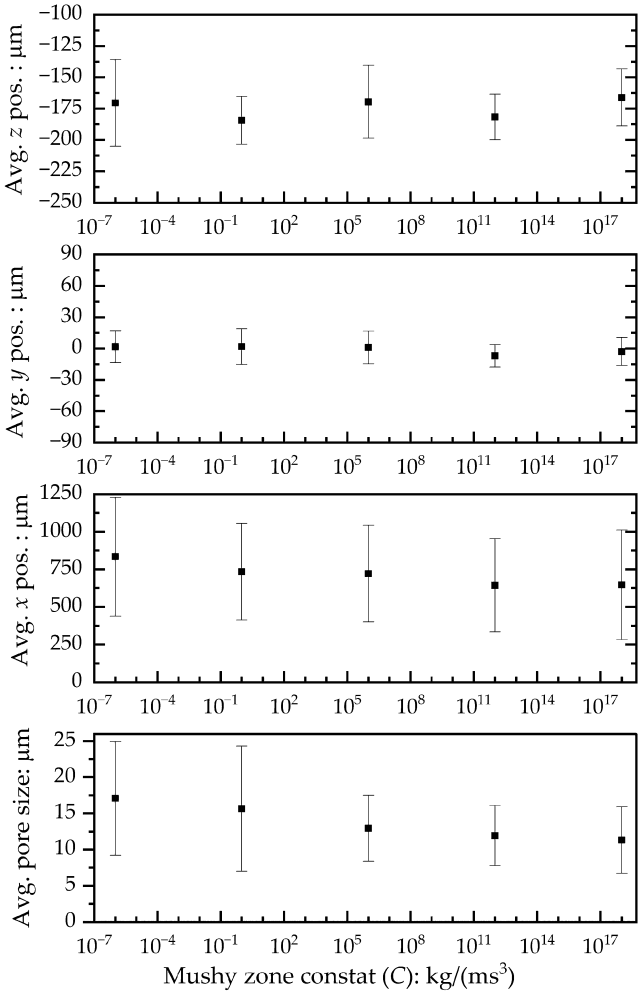

Fig. 9. Influence of mushy zone constant (C) on position and size of pores.

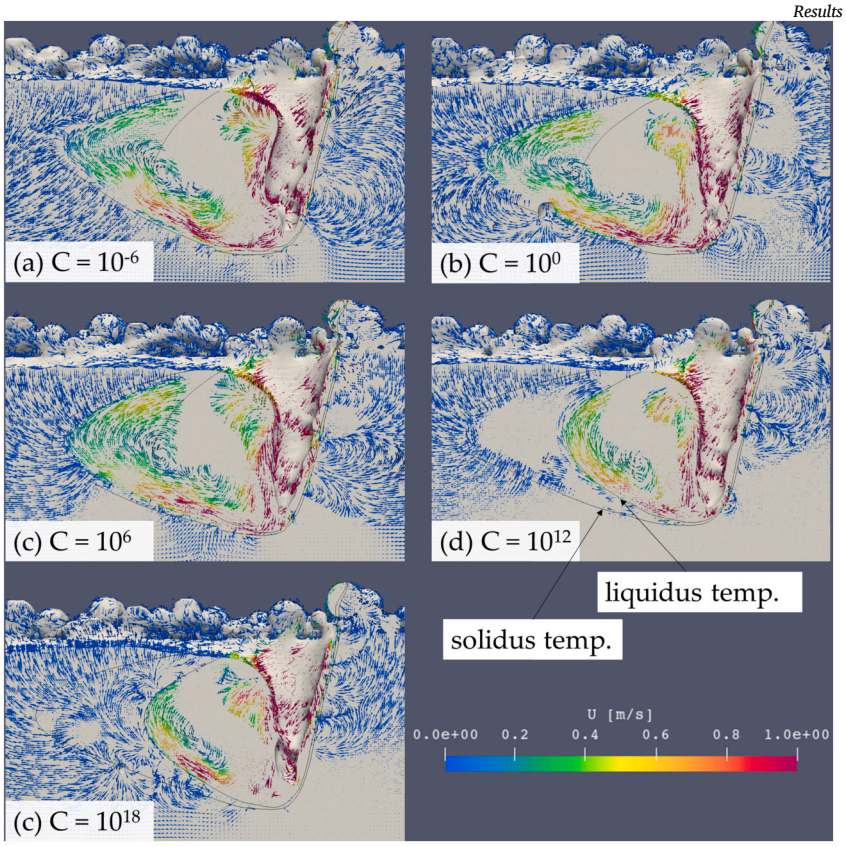

Fig. 10. Velocity distributions in the x-z cross section at $y = 0.15$ mm for the simulation for different C values.

al. suggest that this is due to pressure equalisation. According to the hypothesis of Huang et al., the pores generated in the simulation rapidly change shape. Subsequently, during the cooling process, Huang et al. proposed the hypothesis that the pore diameter shrinks due to condensation of vapour inside the pore. The shape change of the pore immediately after its formation in the molten region: temperature between T_l and T_v. Thereafter, the shape change gradually decreases as the pores pass through the mushy zone. As C is increased, the pores are trapped in the solid before it becomes stable in shape: spherical in most cases. The mushy zone is considered to be the solid metal because of the high flow resistance when $C > 10^6$. Therefore, we assume that the mean and variation of pore size are almost identical when $C > 10^6$. In other words, the dynamics after pore formation will not be reproduced by the simulation using the large C value. By using an appropriate (plausible) value of C, we believe we can reproduce the phenomenon of pore dynamics, i.e. the pores emerge from the molten pool after the shape change and their displacement is gradually slowed down in the mushy zone. In this study, the mushy zone constant of 10^{-6} was proposed. In order to verify the acceptability of this value, it is necessary to carry out experiments and visualisations under the same conditions as the simulation and to evaluate the pore dynamics.

As described above, the Kozeny-Carman equation, which is the basis of the Voller-Prakash model, has been applied to very slow porous flows: Re $\approx$ 1. However, as shown in Fig. 10, the flow velocity at the bottom of the molten pool was high. For such a high flow velocity regime, we should consider the applicability of the Kozeny-Carman equation. The pressure gradient - porosity (liquid fraction) relationship that can be applied to the high flow velocity regime (inertial flow) has been proposed in the past studies, e.g. Ergun's equation [80] and Di Felice's equation [81]. The simulations using the Ergun or Di Felice relations will also be considered in our future task.

In the present study, the mushy zone constants were analytically determined for the simple morphologies. To justify the use of the simple morphologies, we should visualise the real dendrite structure formed in the L-PBF process. However, the L-PBF process is a rapid process and it is difficult to visualise its 3D dendrite structures. It has been confirmed that C is related to pore size, which means that the mushy zone constant, i.e. the solidification morphology, may be determined by back-calculation if the pore size distribution of the L-PBF experiment can be obtained. Until now, it has been difficult to determine the mushy zone constant on the basis of evidence, but the results of the present study have demonstrated the possibility of estimation from the experimental observations. In this study, the laser processing condition was just under a single condition of 300 W and 500 mm/s. We will perform the simulation under the other conditions and also evaluate the pore dynamics in detail in our future work.

This study has focused on the thermo-fluid dynamics behaviour during the L-PBF fabrication process. Following the fabrication using L-PBF, post-processing such as surface finishing is often performed, which can alter the material properties. For example, previous studies have demonstrated that surface modifications due to post-processing can affect the material mechanical properties [82–85]. It should be noted that this study does not assess the effect of such post-processing on the material characteristics.

5. Conclusions

This paper investigates the mushy zone constant of the Voller-Prakash model, which is used in multiphysics CFD simulations involving phase changes, such as LPBF. A drag force model that includes the morphological parameters of the Kozeny-Carman equation is derived, assuming that dynamic and static pressures are equivalent. The model is characterised by the grid size of the simulation, in addition to the morphological parameters. The model assumes three simple morphologies: rectangular, cone, and cone assembly. Their morphological parameters and the mushy zone constant are estimated analytically. The morphological parameters are compared with those obtained in previous studies.

The rectangular morphology is a suitable choice for the proposed drag model. This is because the micrometre-scale grid is commonly used in multiphysics CFD simulations of LPBFs, and the alloy dendrite structure is typically on the scale of a few hundred micrometres to a few millimetres, as observed in past experimental visualisations such as x-ray CT. Furthermore, we have discovered that the mushy zone constant for the rectangular morphology is significantly smaller than the value conventionally used in previous multiphysics CFD simulations.

CRediT authorship contribution statement

Jun Katagiri: Writing – review & editing, Writing – original draft, Visualization, Validation, Methodology, Formal analysis, Data curation, Conceptualization. **Sukeharu Nomoto:** Writing – review & editing, Validation, Methodology, Formal analysis. **Masahiro Kusano:** Writing – review & editing, Validation, Software, Formal analysis. **Makoto Watanabe:** Writing – review & editing, Validation, Supervision, Project administration, Funding acquisition, Formal analysis.

Declaration of competing interest

The authors declare no conflict of interest. The funders had no role in the design of the study; in the collection, analyses, or interpretation of data; in the writing of the manuscript; or in the decision to publish the results.

Acknowledgement

Financial support from Innovative Science and Technology Initiative for Security, Grant Number JPJ004596 implemented by the Acquisition, Technology, and Logistics Agency (ATLA).

Data availability

Data will be made available on request.

References

[1] M.S. Manola, B. Singh, M.K. Singla, J.S. Chohan, R. Kumar, R. Kumar, Y.S. Bisht, R. Kumar, M.Q. Alkahtani, S. Islam, M.I. Ammarullah, M.I. Ammarullah, M.I. Ammarullah, Investigation of melt flow index and tensile properties of dual metal reinforced polymer composites for 3d printing using machine learning approach: biomedical and engineering applications, AIP Adv. 14 (5 2024), https://doi.org/10.1063/5.0207551.

[2] M.H. Ramlee, M.I. Ammarullah, N.S.M. Sukri, N.S.F. Hassan, M.H. Baharuddin, M.R.A. Kadir, Investigation on three-dimensional printed prosthetics leg sockets coated with different reinforcement materials: analysis on mechanical strength and microstructural, Sci. Rep. 14 (12 2024), https://doi.org/10.1038/s41598-024-57454-8.

[3] W.D. Lestari, N. Adyono, A.K. Faizin, A. Haqiyah, K.H. Sanjaya, A. Nugroho, W. Kusmasari, M.I. Ammarullah, Optimization of 3d printed parameters for socket prosthetic manufacturing using the Taguchi method and response surface methodology, Results Eng. 21 (3 2024), https://doi.org/10.1016/j.rineng.2024.101847.

[4] S. Nagaraja, P.B. Anand, K.M. Kumar, M.I. Ammarullah, Synergistic advances in natural fibre composites: a comprehensive review of the eco-friendly bio-composite development, its characterization and diverse applications, RSC Adv. 14 (2024) 17594–17611, https://doi.org/10.1039/d4ra00149d.

[5] A.U.A. Aziz, M.I. Ammarullah, B.W. Ng, H.S. Gan, M.R.A. Kadir, M.H. Ramlee, Unilateral external fixator and its biomechanical effects in treating different types of femoral fracture: a finite element study with experimental validated model, Heliyon 10 (2 2024), https://doi.org/10.1016/j.heliyon.2024.e26660.

[6] R. Seede, D. Shoukr, B. Zhang, A. Whitt, S. Gibbons, P. Flater, A. Elwany, R. Arroyave, I. Karaman, An ultra-high strength martensitic steel fabricated using selective laser melting additive manufacturing: densification, microstructure, and mechanical properties, Acta Mater. 186 (2020) 199–214, https://doi.org/10.1016/j.actamat.2019.12.037.

[7] M.I. Ammarullah, T. Hidayat, M. Danny, P. Lamura, J. Jamari, Relationship between deformation and running-in wear on hard-on-hard bearings from metal, ceramic, and diamond materials for total hip prosthesis, J. Tribol. 38 (2023) 69–81.

[8] Z.F.M. Salaha, M.I. Ammarullah, N.N.A.A. Abdullah, A.U.A. Aziz, H.S. Gan, A.H. Abdullah, M.R.A. Kadir, M.H. Ramlee, Biomechanical effects of the porous structure of Gyroid and Voronoi hip implants: a finite element analysis using an experimentally validated model, Materials 16 (5 2023), https://doi.org/10.3390/ma16093298.

[9] M.I. Ammarullah, R. Hartono, T. Supriyono, G. Santoso, S. Sugiharto, M.S. Permana, Polycrystalline diamond as a potential material for the hard-on-hard bearing of total hip prosthesis: von Mises stress analysis, Biomedicines 11 (3 2023), https://doi.org/10.3390/biomedicines11030951.

[10] G. Santoso, M.I. Ammarullah, S. Sugiharto, R.M. Rachayu, A. Mughni, A.P. Bayuseno, J. Jamari, Von Mises stress analysis of surgery chair designed for laparoscopic surgeon with lifting mechanism, AIP Adv. 14 (4 2024), https://doi.org/10.1063/5.0188663.

[11] G. Santoso, M.I. Ammarullah, S. Sugiharto, T. Hidayat, S. Khoeron, A.P. Bayuseno, J. Jamari, Triz-based method for developing a conceptual laparoscopic surgeon's chair, Cogent Eng. 11 (2024), https://doi.org/10.1080/23311916.2023.2298786.

[12] M. Tauviqirrahman, J. Jamari, S. Susilowati, C. Pujiastuti, B. Setiyana, A.H. Pasaribu, M.I. Ammarullah, Performance comparison of Newtonian and non-Newtonian fluid on a heterogeneous slip/no-slip journal bearing system based on cfd-fsi method, Fluids 7 (7 2022), https://doi.org/10.3390/fluids7070225.

[13] E.R. Babu, N.C. Reddy, A. Babbar, A. Chandrashekar, R. Kumar, P.S. Bains, M. Alsubih, S. Islam, S.K. Joshi, A. Rizal, M.I. Ammarullah, Characteristics of pulsating heat pipe with variation of tube diameter, filling ratio, and sio2 nanoparticles: biomedical and engineering implications, Case Stud. Therm. Eng. 55 (3 2024), https://doi.org/10.1016/j.csite.2024.104065.

[14] A.T. Prakoso, H. Basri, D. Adanta, I. Yani, M.I. Ammarullah, I. Akbar, F.A. Ghazali, A. Syahrom, T. Kamarul, The effect of tortuosity on permeability of porous scaffold, Biomedicines 11 (2 2023), https://doi.org/10.3390/biomedicines11020427.

[15] M. Muchammad, M. Tauviqirrahman, M.I. Ammarullah, M. Iqbal, B. Setiyana, J. Jamari, Performance of textured dual mobility total hip prosthesis with a concave dimple during Muslim prayer movements, Sci. Rep. 14 (12 2024), https://doi.org/10.1038/s41598-023-50887-7.

[16] M. Arun, D. Barik, S.S. Chandran, N. Govil, P. Sharma, T.M.Y. Khan, R.U. Baig, B.J. Bora, B.J. Medhi, R. Kumar, A. Rizal, M.I. Ammarullah, Twisted helical tape's impact on heat transfer and friction in zinc oxide (zno) nanofluids for solar water heaters: biomedical insight, Case Stud. Therm. Eng. 56 (4 2024), https://doi.org/10.1016/j.csite.2024.104204.

[17] M. Bayat, S. Mohanty, J.H. Hattel, Multiphysics modelling of lack-of-fusion voids formation and evolution in in718 made by multi-track/multi-layer l-pbf, Int. J. Heat Mass Transf. 139 (2019) 95–114, https://doi.org/10.1016/j.ijheatmasstransfer.2019.05.003.

[18] L. Wang, Y. Zhang, H.Y. Chia, W. Yan, Mechanism of keyhole pore formation in metal additive manufacturing, npj Comput. Mater. 8 (12 2022), https://doi.org/10.1038/s41524-022-00699-6.

[19] D. Grange, A. Queva, G. Guillemot, M. Bellet, J.D. Bartout, C. Colin, Effect of processing parameters during the laser beam melting of inconel 738: comparison between simulated and experimental melt pool shape, J. Mater. Process. Technol. 289 (3 2021), https://doi.org/10.1016/j.jmatprotec.2020.116897.

[20] A. Queva, G. Guillemot, C. Moriconi, C. Metton, M. Bellet, Numerical study of the impact of vaporisation on melt pool dynamics in laser powder bed fusion - application to in718 and ti–6al–4v, Addit. Manuf. 35 (10 2020), https://doi.org/10.1016/j.addma.2020.101249.

[21] Z. Ren, D.Z. Zhang, G. Fu, J. Jiang, M. Zhao, High-fidelity modelling of selective laser melting copper alloy: laser reflection behavior and thermal-fluid dynamics, Mater. Des. 207 (9 2021), https://doi.org/10.1016/j.matdes.2021.109857.

[22] E.L. Li, L. Wang, A.B. Yu, Z.Y. Zhou, A three-phase model for simulation of heat transfer and melt pool behaviour in laser powder bed fusion process, Powder Technol. 381 (2021) 298–312, https://doi.org/10.1016/j.powtec.2020.11.061.

[23] P. Ninpetch, P. Kowitwarangkul, S. Mahathanabodee, P. Chalermkarnnon, P. Rattanadecho, Computational investigation of thermal behavior and Molten metal flow with moving laser heat source for selective laser melting process, Case Stud. Therm. Eng. 24 (4 2021), https://doi.org/10.1016/j.csite.2021.100860.

[24] T.F. Flint, J.D. Robson, G. Parivendhan, P. Cardiff, laserbeamfoam: laser ray-tracing and thermally induced state transition simulation toolkit, SoftwareX 21 (2 2023), https://doi.org/10.1016/j.softx.2022.101299.

[25] W. Alphonso, M. Baier, S. Carmignato, J. Hattel, M. Bayat, On the possibility of doing reduced order, thermo-fluid modelling of laser powder bed fusion (l-pbf) – assessment of the importance of recoil pressure and surface tension, J. Manuf. Process. 94 (2023) 564–577, https://doi.org/10.1016/j.jmapro.2023.03.040, https://www.sciencedirect.com/science/article/pii/S1526612523002542.

[26] M. Carraturo, B. Lane, H. Yeung, S. Kollmannsberger, A. Reali, F. Auricchio, Numerical evaluation of advanced laser control strategies influence on residual stresses for laser powder bed fusion systems, Integr. Mater. Manuf. Innov. 9 (2020) 435–445, https://doi.org/10.1007/s40192-020-00191-3.

[27] H. Kitano, M. Kusano, M. Tsujii, A. Yumoto, M. Watanabe, Process parameter optimization framework for the selective laser melting of hastelloy x alloy considering defects and solidification crack occurrence, Crystals 11 (2021), https://doi.org/10.3390/cryst11060578, https://www.mdpi.com/2073-4352/11/6/578.

[28] J. Katagiri, M. Kusano, S. Minamoto, H. Kitano, K. Daimaru, M. Tsujii, M. Watanabe, Melt pool shape evaluation by single-track experiments and finite-element thermal analysis: balling and lack of fusion criteria for generating process window of inconel738lc, Materials 16 (2 2023), https://doi.org/10.3390/ma16041729.

[29] V.R. Voller, C. Prakash, A fixed grid numerical modelling methodology for convection-diffusion mushy region phase-change problems, Int. J. Heat Mass Transf. 30 (1987) 1709–1719.

[30] P.C. Carman, Fluid flow through granular beds, Trans. Inst. Chem. Eng. 15 (1937) 150–166, URL citeulike-article-id:5101159.

[31] P.C. Carman, Permeability of saturated sands, soils and clays, J. Agric. Sci. 29 (1939) 262–273, https://doi.org/10.1017/S0021859600051789.

[32] W. Carrier, Goodbye, Hazen; hello, Kozeny-Carman, J. Geotech. Geoenviron. Eng. 129 (2003) 1054–1056, https://doi.org/10.1061/(ASCE)1090-0241(2003)129:11(1054).

[33] S. Tiari, S. Qiu, M. Mahdavi, Discharging process of a finned heat pipe-assisted thermal energy storage system with high temperature phase change material, Energy Convers. Manag. 118 (2016) 426–437, https://doi.org/10.1016/j.enconman.2016.04.025.

[34] H. Shmueli, G. Ziskind, R. Letan, Melting in a vertical cylindrical tube: numerical investigation and comparison with experiments, Int. J. Heat Mass Transf. 53 (2010) 4082–4091, https://doi.org/10.1016/j.ijheatmasstransfer.2010.05.028.

[35] L. Yu, G.L. Ding, J. Reye, S.N. Ojha, S.N. Tewari, G. Ding, S. Ojha, S. Tewari, Mushy zone morphology during directional solidification of pb-5.8 wt pct sb alloy, Metall. Mater. Trans. A 31 (2000) 2275–2285.

[36] M.A. Azeem, P.D. Lee, A.B. Phillion, S. Karagadde, P. Rockett, R.C. Atwood, L. Courtois, K.M. Rahman, D. Dye, Revealing dendritic pattern formation in ni, fe and co alloys using synchrotron tomography, Acta Mater. 128 (2017) 241–248, https://doi.org/10.1016/j.actamat.2017.02.022.

[37] R.H. Mathiesen, L. Arnberg, X-ray radiography observations of columnar dendritic growth and constitutional undercooling in an Al-30wt%Cu, Acta Mater. 53 (2005) 947–956, https://doi.org/10.1016/j.actamat.2004.10.050.

[38] H. Yasuda, K. Morishita, N. Nakatsuka, T. Nishimura, M. Yoshiya, A. Sugiyama, K. Uesugi, A. Takeuchi, Dendrite fragmentation induced by massive-like δ–γ transformation in fe–c alloys, Nat. Commun. 10 (12 2019), https://doi.org/10.1038/s41467-019-11079-y.

[39] G. Reinhart, D. Grange, L. Abou-Khalil, N. Mangelinck-Noël, N.T. Niane, V. Maguin, G. Guillemot, C.A. Gandin, H. Nguyen-Thi, Impact of solute flow during directional solidification of a ni-based alloy: in-situ and real-time x-radiography, Acta Mater. 194 (2020) 68–79, https://doi.org/10.1016/j.actamat.2020.04.003.

[40] S. Karagadde, C.L.A. Leung, P.D. Lee, Progress on in situ and operando X-ray imaging of solidification processes, Materials 14 (5 2021), https://doi.org/10.3390/ma14092374.

[41] M.L.N.M. Melo, E.M.S. Rizzo, R.G. Santos, Predicting dendrite arm spacing and their effect on microporosity formation in directionally solidified al-cu alloy, J. Mater. Sci. 40 (2005) 1599–1609.

[42] Y.M. Wang, T. Voisin, J.T. McKeown, J. Ye, N.P. Calta, Z. Li, Z. Zeng, Y. Zhang, W. Chen, T.T. Roehling, R.T. Ott, M.K. Santala, P.J. Depond, M.J. Matthews, A.V. Hamza, T. Zhu, Additively manufactured hierarchical stainless steels with high strength and ductility, Nat. Mater. 17 (2018) 63–70, https://doi.org/10.1038/NMAT5021.

[43] M. Yang, L. Wang, W. Yan, Phase-field modeling of grain evolutions in additive manufacturing from nucleation, growth, to coarsening, npj Comput. Mater. 7 (12 2021), https://doi.org/10.1038/s41524-021-00524-6.

[44] A. Trykozko, M. Peszynska, M. Dohnalik, Modeling non-Darcy flows in realistic pore-scale proppant geometries, Comput. Geotech. 71 (2016) 352–360, https://doi.org/10.1016/j.compgeo.2015.08.011, http://www.sciencedirect.com/science/article/pii/S0266352X15001883.

[45] R. Sivanesapillai, H. Steeb, A. Hartmaier, Transition of effective hydraulic properties from low to high Reynolds number flow in porous media, Geophys. Res. Lett. 41 (2014) 4920–4928, https://doi.org/10.1002/2014GL060232.

[46] G.A. Narsilio, O. Buzzi, S. Fityus, T.S. Yun, D.W. Smith, Upscaling of Navier–Stokes equations in porous media: theoretical, numerical and experimental approach, Comput. Geotech. 36 (2009) 1200–1206, https://doi.org/10.1016/j.compgeo.2009.05.006, http://www.sciencedirect.com/science/article/pii/S0266352X0900086X.

[47] J. Katagiri, M. Kusano, S. Nomoto, M. Watanabe, Influence of recoil pressure, mushy zone flow resistance and reflectivity on melt pool shape in laser powder bed fusion simulation, Case Stud. Therm. Eng. 50 (2023) 103477, https://doi.org/10.1016/j.csite.2023.103477, https://www.sciencedirect.com/science/article/pii/S2214157X23007839.

[48] M.I. Yuce, D.A. Kareem, A numerical analysis of fluid flow around circular and square cylinders, J. Am. Water Works Assoc. 108 (10) (2016) E546–E554, https://doi.org/10.5942/jawwa.2016.108.0141, https://awwa.onlinelibrary.wiley.com/doi/pdf/10.5942/jawwa.2016.108.0141.

[49] S.F. Hoerner, Fluid-Dynamic Drag, 2nd edition, 1965, Midland Park, N.J., first edition published under the title: Aerodynamic Drag.

[50] J. Katagiri, S. Kimura, S. Noda, Significance of shape factor on permeability anisotropy of sand: representative elementary volume study for pore-scale analysis, Acta Geotech. 15 (2020) 2195–2203, https://doi.org/10.1007/s11440-020-00912-0.

[51] J. Katagiri, Y. Konno, J. Yoneda, N. Tenma, Pore-scale modeling of flow in particle packs containing grain-coating and pore-filling hydrates: verification of a Kozeny–Carman-based permeability reduction model, J. Nat. Gas Sci. Eng. 45 (2017) 537–551, https://doi.org/10.1016/j.jngse.2017.06.019.

[52] E. Li, Z. Zhou, L. Wang, H. Shen, R. Zou, A. Yu, Particle scale modelling of melt pool dynamics and pore formation in selective laser melting additive manufacturing, Powder Technol. 397 (2022) 117012, https://doi.org/10.1016/j.powtec.2021.11.056, https://www.sciencedirect.com/science/article/pii/S0032591021010111.

[53] P. Mostaghimi, M.J. Blunt, B. Bijeljic, Computations of absolute permeability on micro-ct images, Math. Geosci. 45 (2013) 103–125, https://doi.org/10.1007/s11004-012-9431-4.

[54] J.W. Gibbs, K.A. Mohan, E.B. Gulsoy, A.J. Shahani, X. Xiao, C.A. Bouman, M.D. Graef, P.W. Voorhees, The three-dimensional morphology of growing dendrites, Sci. Rep. 5 (7 2015), https://doi.org/10.1038/srep11824.

[55] V. Yufit, F. Tariq, D.S. Eastwood, M. Biton, B. Wu, P.D. Lee, N.P. Brandon, Operando visualization and multi-scale tomography studies of dendrite formation and dissolution in zinc batteries, Joule 3 (2019) 485–502, https://doi.org/10.1016/j.joule.2018.11.002.

[56] E. Khajeh, D.M. Maijer, Numerical determination of permeability of al-cu alloys using 3d geometry from X-ray microtomography, Mater. Sci. Technol. 26 (2010) 1469–1476, https://doi.org/10.1179/174328409X411718.

[57] J. Madison, J.E. Spowart, D.J. Rowenhorst, L.K. Aagesen, K. Thornton, T.M. Pollock, Fluid flow and defect formation in the three-dimensional dendritic structure of nickel-based single crystals, Metall. Mater. Trans. A, Phys. Metall. Mater. Sci. 43 (2012) 369–380, https://doi.org/10.1007/s11661-011-0823-8.

[58] J. Katagiri, S. Nomoto, M. Kusano, M. Watanabe, Particle size effect on powder packing properties and Molten pool dimensions in laser powder bed fusion simulation, J. Manuf. Mater. Process. 8 (4 2024), https://doi.org/10.3390/jmmp8020071.

[59] M.I. Ammarullah, G. Santoso, S. Sugiharto, T. Supriyono, O. Kurdi, M. Tauviqirrahman, T.I. Winarni, J. Jamari, Tresca stress study of cocrmo-on-cocrmo bearings based on body mass index using 2d computational model, J. Tribol. 33 (2022) 31–38.

[60] T. Hidayat, M.I. Ammarullah, E. Saputra, M.D.P. Lamura, C.N. Chethan, R. Ismail, A.P. Bayuseno, J. Jamari, A method for estimating the contact area of a dual-mobility total hip prosthesis, AIP Adv. 14 (1 2024), https://doi.org/10.1063/5.0188638.

[61] T. Hidayat, R. Ismail, M. Tauviqirrahman, E. Saputra, M.I. Ammarullah, M.D.P. Lamura, A.P. Bayuseno, Jamari, Running-in behavior of dual-mobility cup during the gait cycle: a finite element analysis, Proc. Inst. Mech. Eng., H J. Eng. Med. 238 (2024) 99–111, https://doi.org/10.1177/09544119231216023, pMID: 38156402.

[62] M. Tauviqirrahman, M.I. Ammarullah, J. Jamari, E. Saputra, T.I. Winarni, F.D. Kurniawan, S.A. Shiddiq, E. van der Heide, Analysis of contact pressure in a 3d model of dual-mobility hip joint prosthesis under a gait cycle, Sci. Rep. 13 (12 2023), https://doi.org/10.1038/s41598-023-30725-6.

[63] H. Versteeg, W. Malalasekera, An Introduction to Computational Fluid Dynamics: The Finite Volume Method, Pearson Education Limited, 2007, https://books.google.co.jp/books?id=RvBZ-UMpGzIC.

[64] H.G. Weller, G. Tabor, H. Jasak, C. Fureby, A tensorial approach to computational continuum mechanics using object-oriented techniques, Comput. Phys. 12 (6) (1998) 620–631, https://doi.org/10.1063/1.168744, https://pubs.aip.org/aip/cip/article-pdf/12/6/620/7865493/620_1_online.pdf.

[65] J.H. Ferziger, M. Perić, Computational Methods for Fluid Dynamics, Springer-Verlag, Berlin, 1996.

[66] T. Marić, J. Höpken, K.G. Mooney, The OpenFOAM Technology Primer, Zenodo, 2021.

[67] R.U. Putra, H. Basri, A.T. Prakoso, H. Chandra, M.I. Ammarullah, I. Akbar, A. Syahrom, T. Kamarul, Level of activity changes increases the fatigue life of the porous magnesium scaffold, as observed in dynamic immersion tests, over time, Sustainability (Switzerland) 15 (1 2023), https://doi.org/10.3390/su15010823.

[68] J. Jamari, M.I. Ammarullah, G. Santoso, S. Sugiharto, T. Supriyono, M.S. Permana, T.I. Winarni, E. van der Heide, Adopted walking condition for computational simulation approach on bearing of hip joint prosthesis: review over the past 30 years, Heliyon 8 (12 2022), https://doi.org/10.1016/j.heliyon.2022.e12050.

[69] M.I. Ammarullah, G. Santoso, S. Sugiharto, T. Supriyono, D.B. Wibowo, O. Kurdi, M. Tauviqirrahman, J. Jamari, Minimizing risk of failure from ceramic-on-ceramic total hip prosthesis by selecting ceramic materials based on Tresca stress, Sustainability (Switzerland) 14 (10 2022), https://doi.org/10.3390/su142013413.

[70] J. Jamari, M.I. Ammarullah, G. Santoso, S. Sugiharto, T. Supriyono, E. van der Heide, In silico contact pressure of metal-on-metal total hip implant with different materials subjected to gait loading, Metals 12 (8 2022), https://doi.org/10.3390/met12081241.

[71] M.I. Ammarullah, I.Y. Afif, M.I. Maula, T.I. Winarni, M. Tauviqirrahman, I. Akbar, H. Basri, E. van der Heide, J. Jamari, Tresca stress simulation of metal-on-metal total hip arthroplasty during normal walking activity, Materials 14 (12 2021), https://doi.org/10.3390/ma14247554.

[72] T. Hidayat, R. Ismail, M. Tauviqirrahman, E. Saputra, M.I. Ammarullah, M. Danny, P. Lamura, A.P. Bayuseno, J. Jamari, Investigation of mesh model for a finite element simulation of the dual-mobility prosthetic hip joint keywords abstract mesh model element size fea contact pressure von Mises artificial hip joint, J. Tribol. 38 (2023) 118–1401.

[73] M.D.P. Lamura, T. Hidayat, M.I. Ammarullah, A.P. Bayuseno, J. Jamari, Study of contact mechanics between two brass solids in various diameter ratios and friction coefficient, Proc. Inst. Mech. Eng., Part J J. Eng. Tribol. 237 (2023) 1613–1619, https://doi.org/10.1177/14657503221144810.

[74] M.D.P. Lamura, M.I. Ammarullah, T. Hidayat, M.I. Maula, J. Jamari, A.P. Bayuseno, Diameter ratio and friction coefficient effect on equivalent plastic strain (peeq) during contact between two brass solids, Cogent Eng. 10 (2023), https://doi.org/10.1080/23311916.2023.2218691.

[75] M.D.P. Lamura, M.I. Ammarullah, M.I. Maula, T. Hidayat, A.P. Bayuseno, J. Jamari, The effect of load, diameter ratio, and friction coefficient on residual stress in a

hemispherical contact for application in biomedical industry, J. Mater. Eng. Perform. (2024), https://doi.org/10.1007/s11665-024-09330-9.

[76] T. Hidayat, M.I. Ammarullah, R. Ismail, E. Saputra, M.D.P. Lamura, K.N. Chethan, A.P. Bayuseno, J. Jamari, Investigation of contact behavior on a model of the dual-mobility artificial hip joint for asians in different inner liner thicknesses, World J. Orthop. 15 (2024) 321–336, https://doi.org/10.5312/wjo.v15.i4.321.

[77] Y. Cai, H. Heng, F. Li, M. Wang, The influences of welding parameters on the metal vapor plume in fiber laser welding based on 3d reconstruction, Opt. Laser Technol. 107 (2018) 1–7, https://doi.org/10.1016/j.optlastec.2018.05.016.

[78] C. Zhao, N.D. Parab, X. Li, K. Fezzaa, W. Tan, A.D. Rollett, T. Sun, Critical instability at moving keyhole tip generates porosity in laser melting, Science 370 (2020) 1080–1086, https://doi.org/10.1126/science.abd1587.

[79] Y. Huang, T.G. Fleming, S.J. Clark, S. Marussi, K. Fezzaa, J. Thiyagalingam, C.L.A. Leung, P.D. Lee, Keyhole fluctuation and pore formation mechanisms during laser powder bed fusion additive manufacturing, Nat. Commun. 13 (2022) 1170, https://doi.org/10.1038/s41467-022-28694-x.

[80] S. Ergun, Fluid flow through packed columns, Chem. Eng. Prog. 48 (1952) 89–94, https://doi.org/10.1029/JB088iS01p0B353.

[81] R.D. Felice, The voidage function for fluid-particle interaction systems, Int. J. Multiph. Flow 20 (1994) 153–159, https://doi.org/10.1016/0301-9322(94)90011-6, http://www.sciencedirect.com/science/article/pii/0301932294900116.

[82] R. Kodandappa, S. Nagaraja, M.M. Chowdappa, M. Krishnappa, G.S. Poornima, M.I. Ammarullah, Application of the Taguchi method and rsm for process parameter optimization in awsj machining of cfrp composite-based orthopedic implants, Open Eng. 14 (1 2024), https://doi.org/10.1515/eng-2024-0057.

[83] M.U. Farooq, S. Anwar, H.A. Bhatti, M.S. Kumar, M.A. Ali, M.I. Ammarullah, Electric discharge machining of ti6al4v eli in biomedical industry: parametric analysis of surface functionalization and tribological characterization, Materials 16 (6 2023), https://doi.org/10.3390/ma16124458.

[84] K. Mughal, M.P. Mughal, M.U. Farooq, S. Anwar, M.I. Ammarullah, Using nanofluids minimum quantity lubrication (nf-mql) to improve tool wear characteristics for efficient machining of cfrp/ti6al4v aeronautical structural composite, Processes 11 (5 2023), https://doi.org/10.3390/pr11051540.

[85] S. Roseno, M.I. Ammarullah, S. Rohman, F. Kurniawati, T. Wahyudi, A.H.S. Wargadipura, M. Masmui, D. Budiyanto, M.D. Effendi, W. Wahyudin, E. Kalembang, H. Hernawan, S. Subari, S. Habibie, T.P.H. Simanjuntak, H. Santoso, A. Ahmad, A.L. Juwono, The effects of carbon fiber surface treatment by oxidation process for enhanced mechanical properties of carbon fiber/epoxy composites for biomedical application, AIP Adv. 14 (1 2024), https://doi.org/10.1063/5.0183153.